



On pre and post-processing of 3D printed ABS thermoplastic sacrificial pattern for strategic dog teeth

Smruti Ranjan Pradhan¹ · Rupinder Singh¹ · Sukhwant Singh Banwait¹ · Satinder Singh² · Arun Anand³

Received: 15 March 2022 / Accepted: 7 July 2022 / Published online: 20 July 2022
© The Author(s), under exclusive licence to Springer Nature Switzerland AG 2022

Abstract

The fabrication of dental crowns (DC) for humans with fused filament fabrication (FFF) followed by investment casting (IC) has been the commercial practice for the past 20 years. However, little has been reported on FFF-based 3D printing of DC for strategic teeth (ST) of veterinary patients (VP), especially in assembly fit. The present study highlights the detailed methodology for the preparation of acrylonitrile butadiene styrene (ABS) DC master pattern (of mandibular first molar (M1) and maxillary fourth pre-molar (PM4) tooth) of a 3-year-old German shepherd dog as a subject. The PM4-M1 combination as ST has geometrical complexity and is important during mastication, requiring tight tolerance to justify assembly fit. This paper explores the role of FFF-based pre-post-processing variables on the geometrical complexity of DC (M1 and PM4) of a dog while assembly in terms of international tolerance (IT) grades. Results of the study suggest that the best settings of FFF for dimensional accuracy (Δd) and surface hardness of master DC pattern prepared are as follows: low part density, 180° orientation angle, and post-treatment temperature of 80 °C (based upon multifactor optimization). The results from this study are supported by scanning electron microscopy (SEM), 3D rendered images, and surface texture profiles.

Keywords Molar · Pre-molar · Master pattern · Dental crowns · Parametric optimization · 3D printing

1 Introduction

Several novel approaches have been developed in the arena of dental prosthetics in recent years that concede the design and manufacture of précised, custom-specific, and optimal dental restorations [1]. Different additive manufacturing (AM) methods like the lost-wax technique, swaging, electroforming, three-dimensional printing (3DP), and subtractive manufacturing-based milling are used for the manufacturing of different prostheses in dental industries [1, 2]. AM is a skillful method of making parts from computer-aided design (CAD) models by curing, depositing, or attempting to consolidate materials in selective layers [3]. These AM

technologies are pretty more widely applied in a variety of automobile, aerospace, biomedical, construction, engineering, microfluidics, and other application areas to reduce production time for parts to be manufactured with complex features [4]. Over the past few decades, these approaches have been proficiently applied for batch production with mass customization; however, the previously reported studies were limited to developing models for product visualization [5]. CAD/Computer-aided manufacturing (CAM) technologies can provide better clinical treatment for orthodontic patients by acquiring scanned data with complex integrated designs that are then produced using digital technology [6, 7]. The CAD software systems are used in these non-traditional crown designs and manufacturing methods to improve the fit, aesthetics, and versatility of customized parts [8, 9]. The use of CAD/CAM-based AM has a substantial effect on dental restorations for humans. It has been widely reported that for VP like domestic dogs, the ST are interchangeable based on age and breed [10]. As a consequence, batch processing could be a considerable solution (for a particular age/breed of canine), which would minimize the expected downtime.

✉ Rupinder Singh
rupindersingh@nittrchd.ac.in

¹ Department of Mechanical Engineering, National Institute of Technical Teachers Training and Research, Chandigarh, India

² Department of Mechanical Engineering, Punjab Engineering College (Deemed to be University), Chandigarh, India

³ Department of Veterinary Surgery and Radiology, GADVASU, Ludhiana, India

The FFF is a low-cost AM method that uses thermoplastic feedstock to fabricate the parts from a virtual solid model. The working mechanism starts with the development of a three-dimensional virtual solid model [11, 12]. Many commercial CAD packages are used to do this. The model is then exported in the stereolithography (STL) format to the FFF software (such as Catalyst EX). After being exported to Catalyst, the STL file is horizontally fragmented into several thin segments. These parts reflect the FFF process's two-dimensional topography, which, when layered on top of one another, strongly matches the original three-dimensional segment. The Catalyst software then uses this information to generate a process plan that controls the FFF machine's hardware. A solid filament of ABS as model material and polycarbonate (PC) as support material are usually fed via a heating element and turn out to be semi-molten during the fabrication process inside the extruder. The fused filament is then deposited onto the built plate through a nozzle. Since the material is extruded in a semi-molten state, the newly deposited material fuses with neighboring material that has already been deposited. After that, the extruder head moves in the x - y plane, depositing material according to the component's geometry. After this, the built platform, along with the deposited portion of the component, starts moving downward in the z -plane to start consolidating a new layer of fused material on top of the previously deposited surface [13, 14]. In FFF, the semi-molten ABS or any thermoplastic material is consolidated in a criss-cross pattern on the X - Y plane, resulting in porosity between the direction of filament deposition. The infilled densities can be adjusted as sparse low/sparse high/solid before giving the command for printing. Similarly, the selection of orientation angle plays a vital role as it depends on the complexity in the geometry of the part to be printed. Anisotropic mechanical properties are prevalent in AM techniques that manufacture the component layer by layer. The mechanical behavior of FFF specimens was found to be reliant on raster orientation, which is directly related to the build orientation, processing parameters—air gap, layer thickness during printing, and raster width—for materials like ABS [15]. As per reported literature, the raster angle and air gap have more effect on the strength of FFF components. The periodic cellular core structure is commonly used to reduce the weight of printable pieces. With innovative infilled core designs, weight reduction has become a challenge in recent years with less manufacturing cost of cellular structures [16]. FFF has many benefits in general, including limitless shape complexity, a wide range of materials to choose from, nontoxic materials, a quick processing time, easy material changes, low-temperature process, little or no monitoring during part building, lightweight machine, and low maintenance requirements. Because it uses a layered manufacturing technique to produce the needed 3D parts directly from CAD files, one of the

major downsides of FFF technology is the seam lines that emerge between any two neighboring strands. By default, this behavior results in excessive surface roughness (R_a) or even poor adhesion between two layers. Another notable disadvantage of FFF is the limited thermal conductivity of the plastic materials employed. Furthermore, the relatively poor heat tolerance of plastic FFF parts prevents FFF technology from being widely used in many fields [17, 18].

Numerous studies on the production of DC for humans have revealed the use of both conventional and novel AM methods. However, limited work has been recorded for VP, especially in the preparation of DC. A carnivorous animal like a dog may suffer numerous injuries in the duration of its life, but the tooth fracture, particularly injury of the ST, is thought to be devastating [19, 20]. Periodontic treatment for VP is often expensive and requires a massive recovery period. Prosthodontic therapy on VP is initiated at an early stage, either as a preventive strategy or as an accident recovery technique, to remove any need for periodontic treatment [21, 22]. The prosthodontic procedure involves the placement of DC, which is mainly used to avoid trauma or damage in injuries [23]. In commercial practices, for crown therapy, the veterinary surgeon has to initially go for endodontic treatment. For example, in VP, if there is a tooth fracture and for the repair of such fracture the pulp cavity exposure is there, endodontic treatment is the first stage followed by crown fitment to manage the high biting force of dog [20].

The Canidae family of animals, which includes dogs, wolves, and foxes, is of particular interest to this study. Because of the principle of DC interchangeability, the study was limited to dogs (*Canis lupus familiaris*). It should be noted that dogs have two sets of teeth: 28 deciduous teeth that have been extracted when the dog (is 1.5–2 months of its age), and over time, 42 adult teeth that are fully replaced (when they are six or seven months old). The final teeth comprise incisors, which are applied to nip and nibble; canines, which rip and cut into a strip of flesh; and premolars and molars that help in shearing and crushing of foods. Eight teeth are considered to be ST out of the 42 finally grown-up teeth. The total ST is equally divided into mandible and maxilla. These ST are comprised of two canines and M1 in the lower mandible, two canines, and two PM4 in the upper maxilla [24, 25]. The four ST on the left side of the mandible and maxilla are shown in Fig. 1. The other four ST are available on the right side. Due to the value function of ST, tooth loss (partial or fully) may lead to a change in feeding habits and loss of weight in a particular dog. Commercially dental restorative work by veterinarians is manual in nature but recent advancements in technology (such as the use of virtual/ augmented reality tools) may be used to perform these functions digitally [26, 27].

The literature review reveals that fabrication of DC for humans with FFF followed by IC has been the commercial

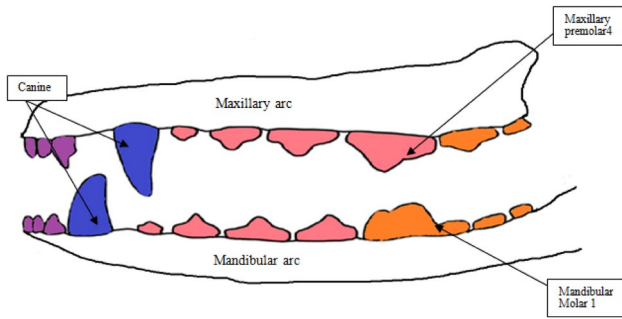


Fig. 1 Schematic of longitudinally cut left half section of maxilla and mandible

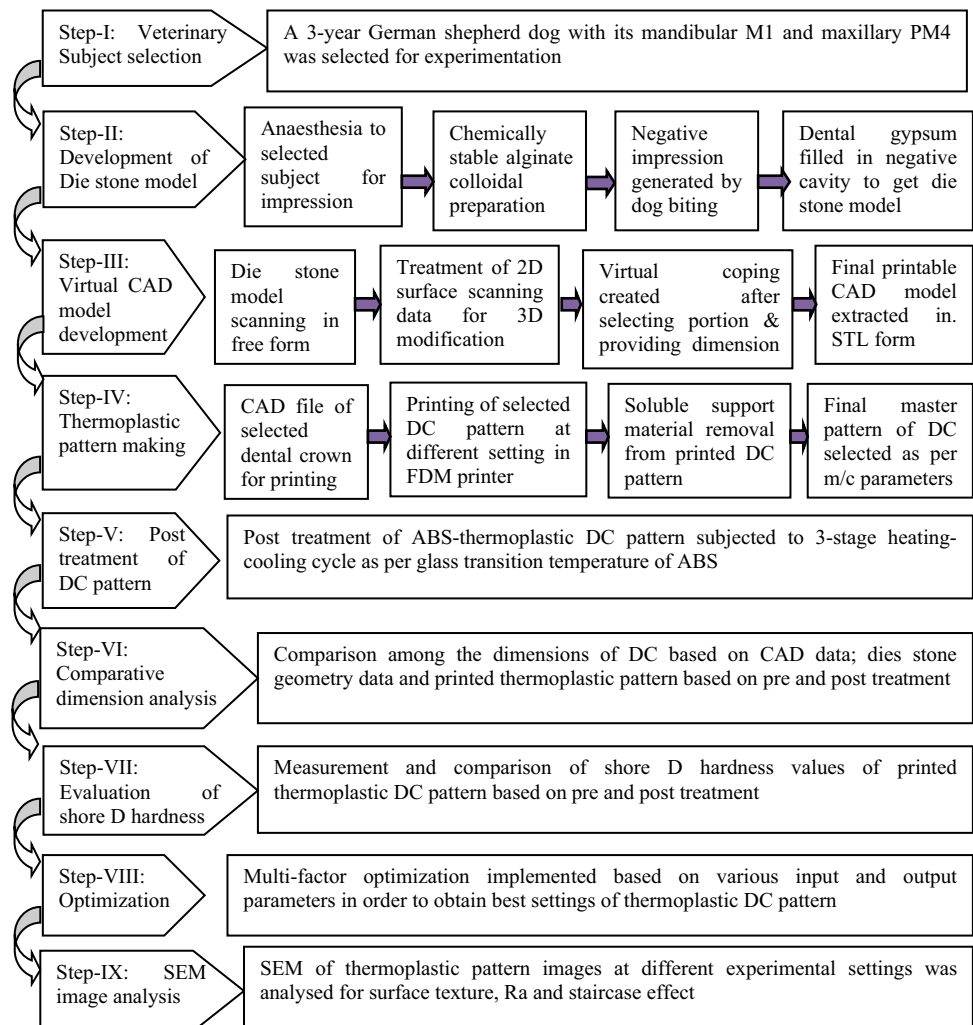
practice for the past 20 years. However, little has been reported on FFF-based 3D printing of DC for ST of VP, especially in assembly fit. The present study highlights the detailed methodology for the preparation of the master DC pattern (M1 and PM4) of a 3-year-old German shepherd dog as a subject. The PM4-M1 combination as ST has

geometrical complexity and is important during mastication, thus requiring tight tolerance to justify assembly fit. This paper explores the role of FFF-based pre-post processing variables on the geometrical complexity of DC (M1 and PM4) of a dog while assembly in terms of IT grades.

2 Methodology

The methodology articulated for maxillary PM4 and mandibular M1 of dogs is shown in Fig. 2. In the recent past, several studies have been carried out to analyze, model, and develop the relation for processing parameters on Δd , R_a , and surface hardness of ABS-based thermoplastic DC pattern printed by FFF [28]. But for assembly fit of different ST, limited studies have been reported. Due to geometrical similarities in the curvature of M1 and PM4 (as ST), left mandibular M1 was considered in this study. The steps for resolving the current problem are as follows:

Fig. 2 An adopted methodology for optimized setting of FFF-based 3D printing for the master pattern of DC



The final part of process optimization includes pre-processing of CAD data for optimum design of CAD file, selection of process parameters to increase adhesion among layers during printing with optimum printing direction for improving surface characteristics of the printed part, and slicing strategy to minimize staircase effect, again, further processing of printed parts to improve surface hardness, microstructure.

3 Experimentation

3.1 Development of CAD data from die stone model

3D imaging through scanning is regarded as an early phase in reverse engineering for the acquisition of surface data [29]. Scanning speed, range of measuring field, speed, and continuity in the scanning of a physical model to get the surface geometry plays a vital role in the generation of a 3D virtual CAD model. Small measuring volumes may be selected with adequate resolution as per environment/surrounding by a skilled operator for preparing object surface [30–32]. Figures 3 and 4 show the development of a virtual CAD model of crown/coping of ST of M1 and PM4 of German shepherd dog. After selecting a 3-year German shepherd dog, alginate as colloidal material for impression making due to dog bite with the help of anesthesia, dental gypsum/die stone for filling impression cavity to get die

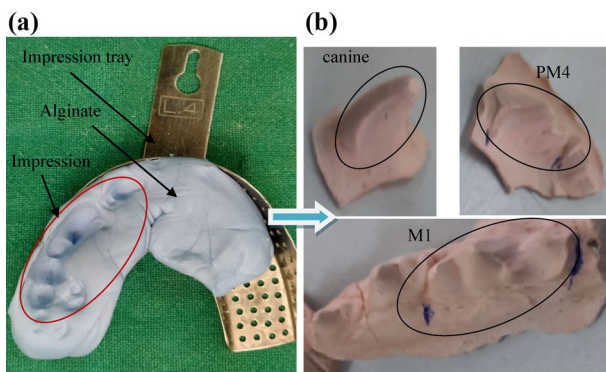
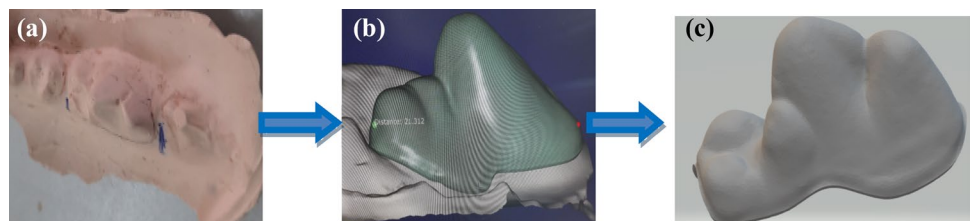


Fig. 3 **a** Impression making in alginate on the dental tray, **b** Die stone models of canine, PM4, and M1

Fig. 4 **a** Die stone model of M1, **b** Coping selected in scanned image in software, **c** .STL file of coping of M1



stone model was performed. Commercial dedicated 3-shape dental software was selected for generating surface data of a dental die stone model of a jaw with teeth. After this 2D surface scanned data were processed in a dental prosthetic design (Delcam CAD/CAM) software of fitting restorations for generation 3D CAD model of coping/crown of two M1 (left and right) of mandible and PM4 (left and right) of the maxilla. These four 3D CAD models were further processed by physical verification with a die stone model by providing a thickness of 0.6 mm to the final crown of the selected ST and restored as '.STL file' after counter verifying with 3-shape dental software.

3.2 3D Printing of a thermoplastic pattern of M1

The sacrificial pattern of the selected ST (left mandibular M1) has been chosen as the benchmark in this study (out of two ST due to almost similarity in geometrical complexity of M1 and PM4). For making the final thermoplastic master pattern of M1, the investigation is alienated into eight steps starting with a benchmark and varying parametric settings (of selected ST). After receiving the validated printable CAD file, the specific ST (M1) was loaded into the FFF printer's CatalystEX software (version 4.3) for slicing. The density (model interior), support fill, no. of copies, STL unit, STL scale, and orientation were chosen followed by slicing and adding the file of M1 into a pack. The print option was then selected for printing CAD files in the FFF printer. At three different densities (sparse low, sparse high, and solid), the printing was performed by changing the orientation angles (120°, 150°, and 180°) with X-axis. The inbuilt program provides information regarding the number of layers, model, and support feedstock material consumption out of available volumes of feedstock in the material bay, as well as the total built time on that particular experimental setting. In this study, P430 (ABS Model material) and P400-SR (Soluble support material) as feedstock filament supplied by Stratasys, USA have been used. The soluble P400-SR support materials were removed from the interior parts of the geometrically complex printed DC with the help of an ultrasonic-assisted stirrer. The 3D printing process flow of thermoplastic DC of M1 by FFF printer is described in Fig. 5. Design of experiment (DOE) based on Taguchi L9 orthogonal array (O.A) was used for the final printing of

Fig. 5 Process flow of thermo-plastic printing of DC of M1

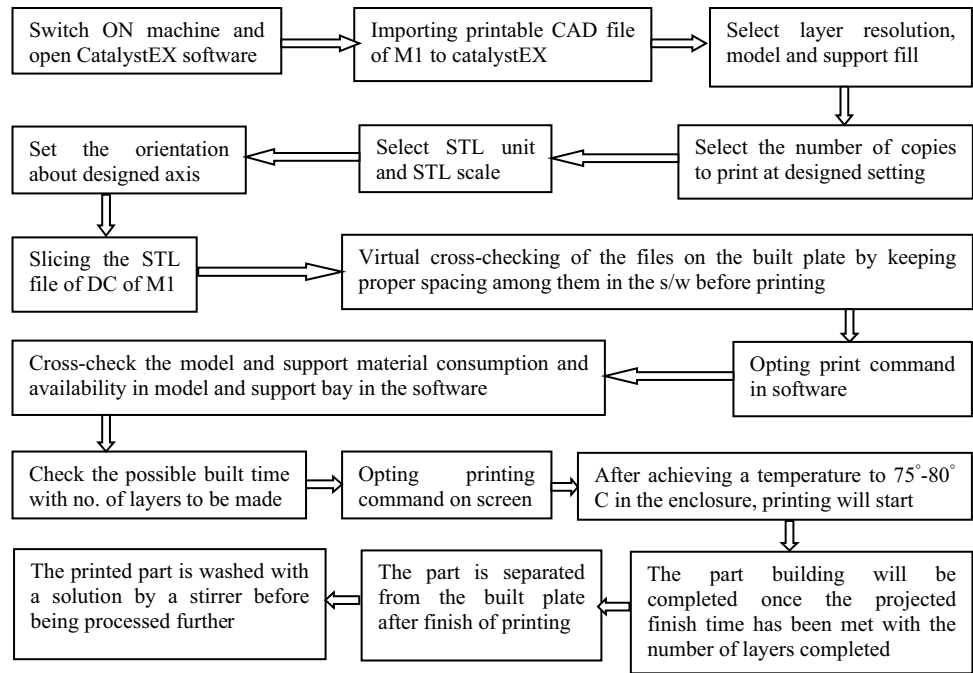


Table 1 Observations during printing (pre-processing stage) (based upon Taguchi L9 OA)

S. no.	Input parameters fixed at the operator level		Observations based upon FDM software and printed parts at the pre-processing stage		
	Part density	Orientation angle along the x-axis	Volume of model material used in DC (in ³)	Weight of DC pattern after cleaning in g	Density of model material (g/in ³)
1	Sparse low	120°	0.028	0.4312	1.5401
2	Sparse low	150°	0.030	0.4246	1.4153
3	Sparse low	180°	0.031	0.4344	1.4013
4	Sparse high	120°	0.028	0.3950	1.4107
5	Sparse high	150°	0.030	0.4233	1.4110
6	Sparse high	180°	0.031	0.4336	1.3987
7	Solid	120°	0.028	0.4395	1.5696
8	Solid	150°	0.030	0.4374	1.4580
9	Solid	180°	0.031	0.4398	1.4187

Fig. 6 **a** Slicing and orientation of CAD file showing the model and support to be consumed, **b** final thermoplastic pattern of DC of M1

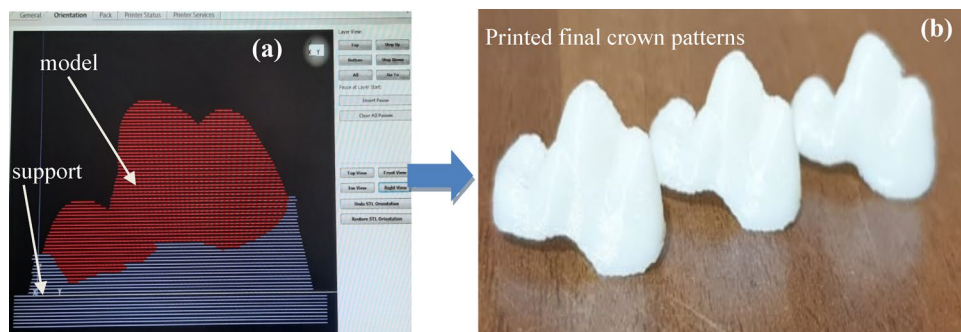


Table 2 Specification of virgin ABS (P430)

Layer thickness	0.254 mm
Color	White
Specific gravity	1.04
Rockwell hardness	109.5
Coefficient of thermal expansion	8.82×10^{-5} mm/mm/°C
Glass transition temperature	108 °C
Heat deflection	82–96 °C
Flexural modulus	1650 MPa
Flexural strain	2%
Tensile modulus	2200 MPa
Tensile elongation	2% at break and 6% at a yield
Impact (IZOD)	106 J/m

thermoplastic patterns of DC for M1 (Table 1). Figure 6 shows the slicing and orientation of the CAD file and the final printed thermoplastic pattern of DC for M1. The specification of ABS used in this experiment is given in Table 2.

3.3 Biomechanics of M1 and PM4

The various forces like compressive, shear, and tear act simultaneously on different points and areas of ST during the action of tearing, chewing, biting, eating, and grinding of food [33]. So, mechanical properties like elastic modulus, brittleness, hardness, ductility, etc. of flesh/ food affect the jaw movement along with the teeth of a dog. Thus, analysis of the different types of forces on teeth and possible moments generated due to movement of the jaw affect the longevity and retentivity of final DC as well as minimize

the abfraction of teeth [34, 35]. The distance D_1 and D_2 and moments M_a and M_b as per reference points of application of force in the co-ordinate system (positioned at the center of both arcs) that measure the angle according to the rotation of maxillary and mandibular arc for calculation of moments are shown in Fig. 7. Also, buccal–lingual (B–L), mesial–distal (M–D), and occlusal–gingival (O–G) axial directions are used for force and moment analysis by previous authors [33–37]. It has been reported that the rate of movements on an occlusal plane can be calculated along the M–D direction [37].

In professional practice, the height, length, and thickness of DC are considered significant for the resistance/retention purpose in minimization of adhesion/cohesion failure rate of ST. In other words, the contour of teeth,

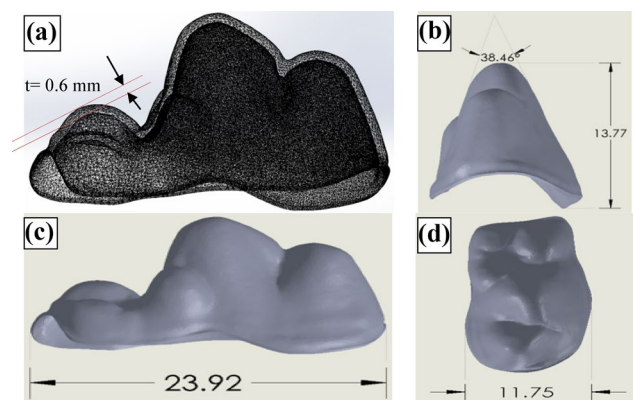


Fig. 8 Measurement of the thickness (a), height and angle (b), length (c), width (d) of CAD file of M1 (linear dimensions are in mm and angle in degree)

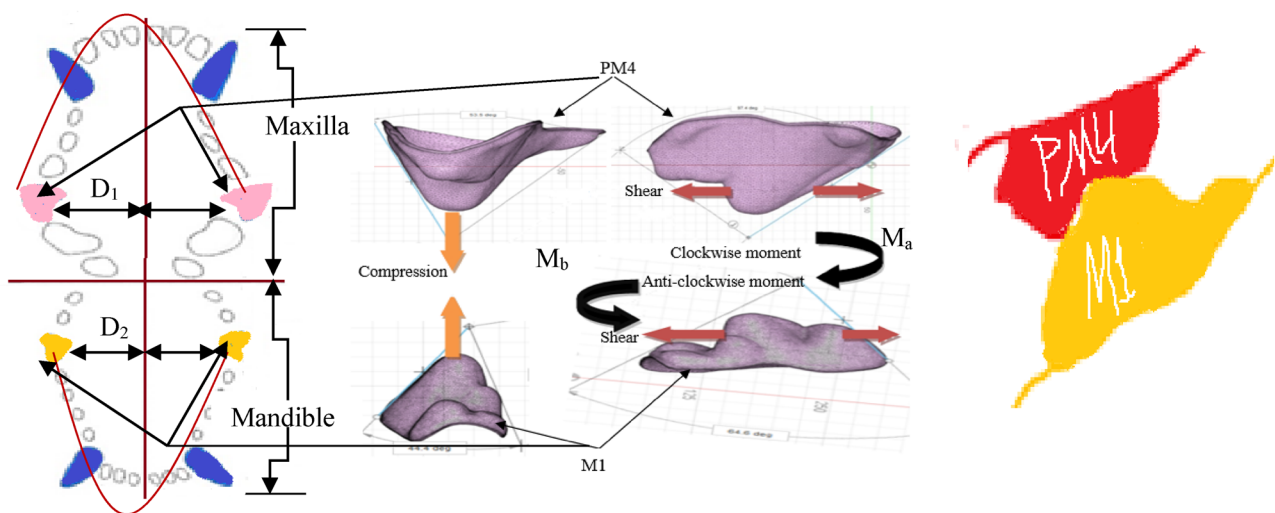


Fig. 7 Force and couple analysis between M1 and PM4 as per their mating (biomechanics of teeth). Note: In this study, occlusal forces were not studied, so full die stone models for maxillary and man-

dibular arc were not prepared. Only individual tooth study has been performed for fabrication purpose, but for future application, clinical studies need to be performed on a standardized dental tray model

Table 3 Calculated IT grades for D_{JN} 23.92 mm

S. no.	D_{JN} (mm)	D_{JM} (mm)	Deviation in mm	i	n	Grade
1	23.92	23.37	0.55	1.29	426.35	IT13 to IT14
2	23.92	23.5	0.42	1.29	325.5	IT12 to IT13
3	23.92	23.75	0.17	1.29	131.78	IT11 to IT12
4	23.92	23.5	0.42	1.29	325.5	IT12 to IT 13
5	23.92	23.5	0.42	1.29	325.5	IT12 to IT13
6	23.92	23.78	0.14	1.29	108.5	IT10 to IT11
7	23.92	23.7	0.22	1.29	170.54	IT11 to IT12
8	23.92	23.7	0.22	1.29	170.54	IT11 to IT12
9	23.92	23.6	0.32	1.29	248.06	IT12 to IT13

Table 4 Calculated IT grades for D_{JN} 11.75 mm

S. no.	D_{JN} (mm)	D_{JM} (mm)	Deviation in mm	i	n	Grade
1	11.75	11.7	0.05	1.29	46.72	IT9 to IT10
2	11.75	11.76	0.01	1.29	9.34	IT5 to IT6
3	11.75	11.72	0.03	1.29	28.03	IT8 to IT9
4	11.75	11.82	0.07	1.29	65.42	IT9 to IT10
5	11.75	12.07	0.32	1.29	299.06	IT13 to IT14
6	11.75	12.03	0.28	1.29	261.68	IT12 to IT13
7	11.75	11.76	0.01	1.29	9.34	IT5 to IT6
8	11.75	11.8	0.05	1.29	46.72	IT9 to IT10
9	11.75	11.9	0.15	1.29	140.18	IT11 to IT12

area of contact between teeth, cementation gap, etc. plays a vital role in the resistance, misfit evaluation, and biomechanics of DC [38, 39]. The convergence angle of the left M1 (CAD file) was measured as 38.46° (Fig. 8) by using devoted CAD software (in the present study). The thickness of the crown measured was fixed as 0.6 mm, height 13.77 mm in CAD data (Fig. 8). Based upon Tables 1, 3 and 4, respectively, show measured dimensions corresponding to the selected nominal dimension as per Fig. 8.

The IT grade system was employed for tolerance examination of the FFF printed DC for ST. Linear dimensions of parallel opposite faces of DC were measured (with three repetitions as per Table 1). FFF process was observed to be capable of printing suitable DC patterns with IT grade varying from IT 11 to IT 14 (lengthwise) and IT 5 to IT 14 (width) wise (Tables 3, 4). Because of observed IT grades, the FFF process is ideal for both concept modeling and assembly applications. The following formulas and calculations for IT grade evaluation are given below [40]:

$$i = 0.45 \times D^{1/3} \pm 0.001 \times D = 1.29 \tag{1}$$

$$n = 1000(D_{JN} - D_{JM})/I \tag{2}$$

$$\text{Geometric mean} = D = (18 \times 30)^{1/2} = 23.23 \text{ mm}, \tag{3}$$

where n , tolerance unit; i , standard tolerance factor; D_{JN} , nominal dimension; D_{JM} , measured dimension.

$$i = 0.45 \times D^{1/3} \pm 0.001 \times D = 1.07 \tag{4}$$

$$n = 1000(D_{JN} - D_{JM})/I \tag{5}$$

$$\text{Geometric mean} = D = (10 \times 18)^{1/2} = 13.41 \text{ mm}.$$

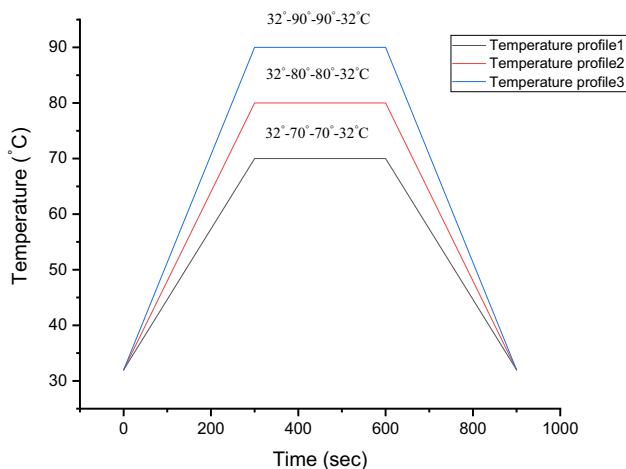
3.4 Post-processing of master patterns

After removal of support material from the printed samples at different settings, three samples at each setting based upon DOE (Table 5) were used for post heat treatment below glass transition temperature (T_g) of ABS ($T_g = 105 \text{ }^\circ\text{C}$ [41–44]). The thermodynamic heating–cooling cycle comprises three temperature profiles that were used. In temperature profile 1, the temperature was raised from room temperature (32 °C) to 70 °C for samples fabricated in experiments 1, 6, and 8 (sensible heating) in 300 s as per Table 5. After this, the same samples were held in reserve at 70 °C for 300 s. Finally, the same samples were brought to 32 °C in the

Table 5 DOE for pre and post-processing of master patterns

S. no.	Part density (A)	Orientation angle (Along <i>x</i> -axis) (B)	Post printing temperature (C) (°C)
1	Sparse low	120°	70
2	Sparse low	150°	80
3	Sparse low	180°	90
4	Sparse high	120°	80
5	Sparse high	150°	90
6	Sparse high	180°	70
7	Solid	120°	90
8	Solid	150°	70
9	Solid	180°	80

For input parameter, A three levels (1, 2, 3) were selected as Sparse low, Sparse high, and Solid based upon availability on FDM setup. For input parameter, B three levels (1,2,3) were selected as 120°, 150°, and 180° based upon availability on FDM setup and pilot experimentation. For input parameter C three levels (1,2, 3) were selected as 70 °C, 80 °C, and 90 °C based upon T_g of ABS and pilot experimentation

**Fig. 9** Temperature vs time plot for different temperature profiles

300 s. Similarly, the 32°–80°–80°–32° C cycle was used for samples fabricated in experiments 2, 4, and 9 (temperature profile2), and the 32°–90°–90°–32° C cycle (temperature profile3) was chosen for samples fabricated in experiment 3, 5, and 7 (Fig. 9).

4 Results and discussion

Table 6 presents the measured results for Shore *D* hardness and dimensional measures based on Table 5. Considering thickness (*t*) (Fig. 8a) as the most critical factor for the

final assembly of DC, the Δd has been calculated on the thickness of the functional part. The signal-to-noise (SN) ratio for the hardness and Δd values of the master pattern were optimized for the larger the better type case and the smaller the better type case, respectively.

SN ratios can be determined as follows[28–30]:

for the larger the better type case

$$\eta = -10 \log \left[\frac{1}{n} \sum_{k=1}^n \frac{1}{y^2} \right] \quad (6)$$

SN ratios can be determined as follows for the smaller the better type case:

$$\eta = -10 \log \left[\frac{1}{n} \sum_{k=1}^n y^2 \right], \quad (7)$$

where η , SN ratio; *n*, the no. of experiment; *y*, the material properties at experiment no. *k*.

Further SN ratio for Shore *D* hardness AHT and Δd_1 has been taken for calculation using Minitab 19 software (based on Table 6). This was because, to commercially fabricate DC via IC, the operator requires a master pattern with an adequate hardness to manage the pressure of slurry coating during IC. As a result, the SN ratio for the hardness obtained AHT was computed for optimization purposes. Another important criterion was the quality of the master pattern, which would be represented in the final cast. As a result, the SN ratio in the form of Δd_1 was determined. Based on Table 6, Fig. 10 presents main effect plots for SN ratios, Shore *D* hardness AHT, and Δd_1 .

Table 7 displays the analysis of variance (ANOVA) for Shore *D* hardness AHT (for larger the better type case) and Δd_1 (for smaller the better type case) based on SN ratio calculations (as per Table 6). The best settings for Shore *D* hardness are component density solid, orientation angle 180°, and post-treatment temperature 80 °C, as shown in Fig. 10a. Higher part density leads to a more thermally stable master pattern; therefore, this setting is but obvious solution. The 180° orientation angle may have resulted in better layer deposition. To put it another way, it may have resulted in a superior surface texture, R_a . Because the post-treatment temperature was near the T_g of ABS, it may have resulted in better processing conditions. However, according to ANOVA analysis (Table 7), only part density is a significant factor with a contribution of 80.25% at the 95 percent confidence level. In terms of Δd_1 , the optimal settings are low part density, 150° orientation angle, and 90 °C post-treatment temperature. Lower density, 150° orientation, and 90 °C temperature (being near to T_g) resulted in a more dimensionally stable master pattern. The ANOVA analysis (Table 7) reveals that for Δd_1 only component density is

Table 6 Observed values of Shore *D* hardness and Δd

S. no.	Shore <i>D</i> hardness			Dimensional measurement		Δd_0	Δd_1	Δd_2	SN ratio for Shore <i>D</i> hardness AHT (dB)	SN ratio for Δd_1 (dB)		
	BHT	AHT	ΔH	BHT							AHT	
				t_1	t_2						t_1	t_2
1	58	60.5	2.5	0.675	0.615	0.075	0.015	0.06	35.6351	36.4782		
2	51.5	57.5	6	0.67	0.61	0.07	0.01	0.06	35.1934	40.0000		
3	62.5	64	1.5	0.665	0.61	0.065	0.01	0.055	36.1236	40.0000		
4	60	63.5	3.5	0.615	0.615	0.015	0.015	0.00	36.0555	36.4782		
5	52.5	56.5	4	0.635	0.61	0.035	0.01	0.025	35.0410	40.0000		
6	58	61.5	3.5	0.66	0.62	0.06	0.02	0.04	35.7775	33.9794		
7	69	73	4	0.65	0.645	0.05	0.045	0.005	37.2665	26.9357		
8	60	69.5	9.5	0.655	0.65	0.055	0.05	0.005	36.8397	26.0206		
9	72.5	74.5	2	0.655	0.64	0.055	0.04	0.015	37.4431	27.9588		

All dimensions in mm. The experiment was performed three times and average values have been reported. BHT, before heat treatment; AHT, after heat treatment; t_1 , thickness BHT; t_2 , thickness AHT (as per Fig. 8); ΔH =difference in hardness BHT and AHT; $\Delta d_0=(t-t_1)$ (difference between thickness as per CAD file data ($t=0.6$ mm) and observed values in different experiments BHT); $\Delta d_1=(t-t_2)$ (Difference between thickness as per CAD file data ($t=0.6$ mm) and observed values in different experiments AHT); $\Delta d_2=\Delta d_1-\Delta d_0$

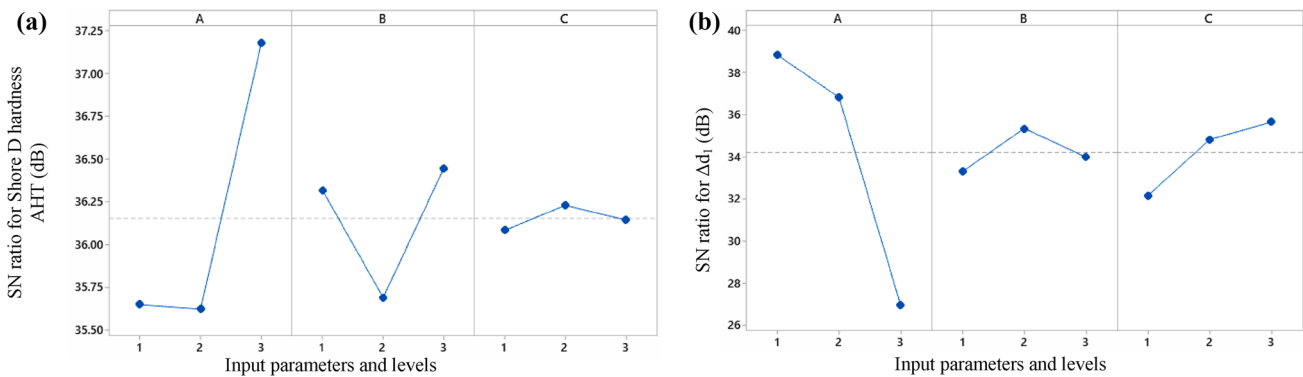


Fig. 10 Main effect plots for SN ratios Shore *D* hardness AHT and Δd_1 based upon Table 5

Table 7 ANOVA for SN ratios

Source	DF	For Shore <i>D</i> hardness AHT				For Δd_1			
		Seq SS	<i>F</i>	<i>P</i>	% <i>C</i>	Seq SS	<i>F</i>	<i>P</i>	% <i>C</i>
A	2	4.77769	29.99	0.032	80.25	241.526	116.44	0.009	89.46
B	2	0.98328	6.17	0.139	16.51	6.490	3.13	0.242	2.40
C	2	0.03259	0.20	0.830	0.54	19.883	9.59	0.094	7.36
Residual Error	2	0.15932			2.67	2.074			0.76
Total	8	5.95288				269.973			

DF, degree of freedom; Seq SS, sequential sum of squares; *F*, Fisher’s value; *P*, probability; %*C*, percentage contribution

a significant parameter with 89.46% contribution at a 95% confidence level.

Table 8 shows the scanning electron microscopy (SEM) images, 3D rendered images, and surface texture profiles for samples AHT (as per Table 6). As observed from

Table 8, R_a values obtained were very close in all settings also, an almost similar surface texture was noticed for all settings of FFF parameters (pre and post-processing). Another important observation from SEM images (Table 8) was that for low-density patterns, uniform layer

Table 8 SEM images, 3D rendered images, and surface texture profiles for samples AHT (as per Table 6)

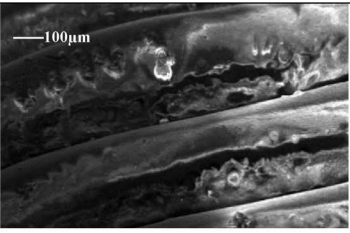
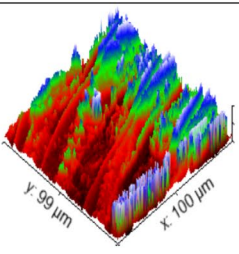
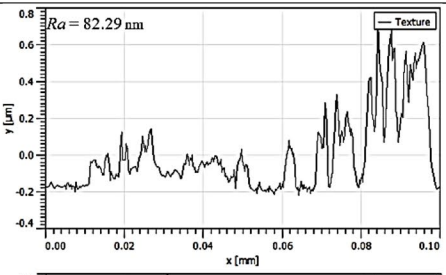
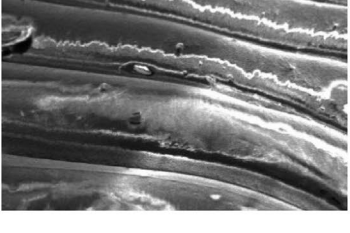
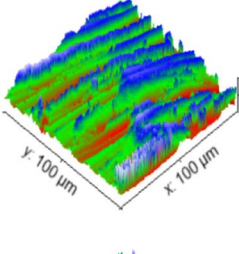
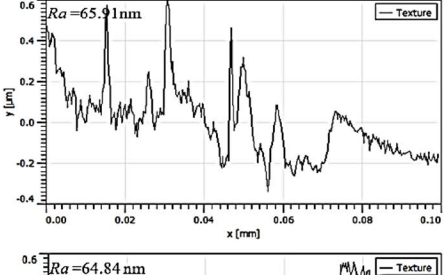
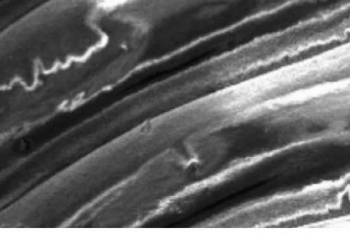
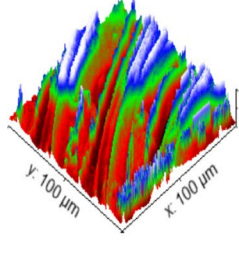
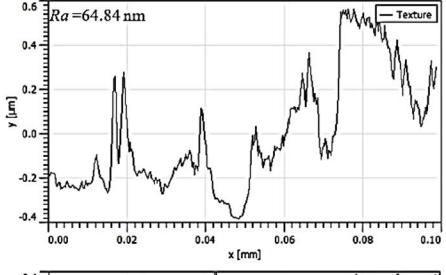
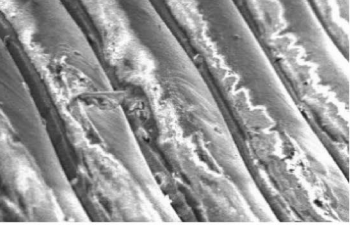
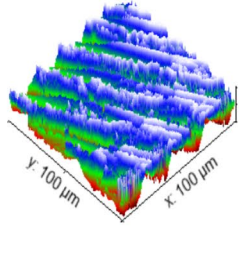
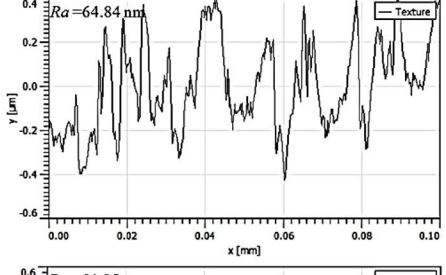
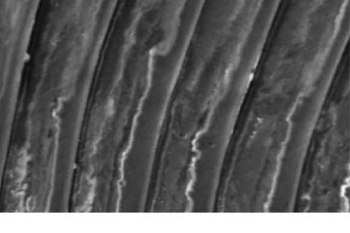
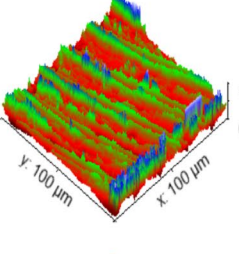
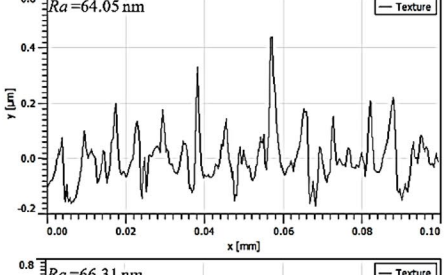
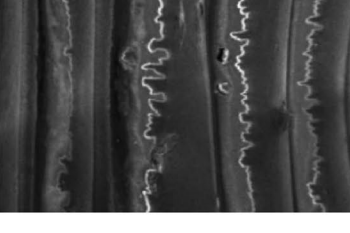
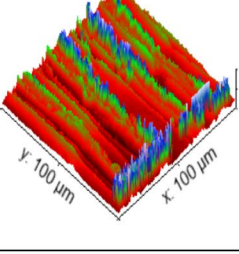
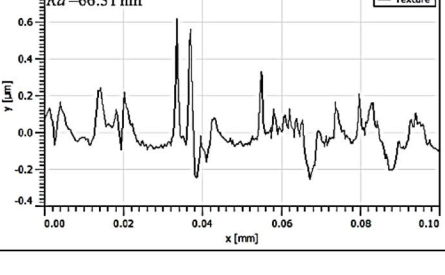
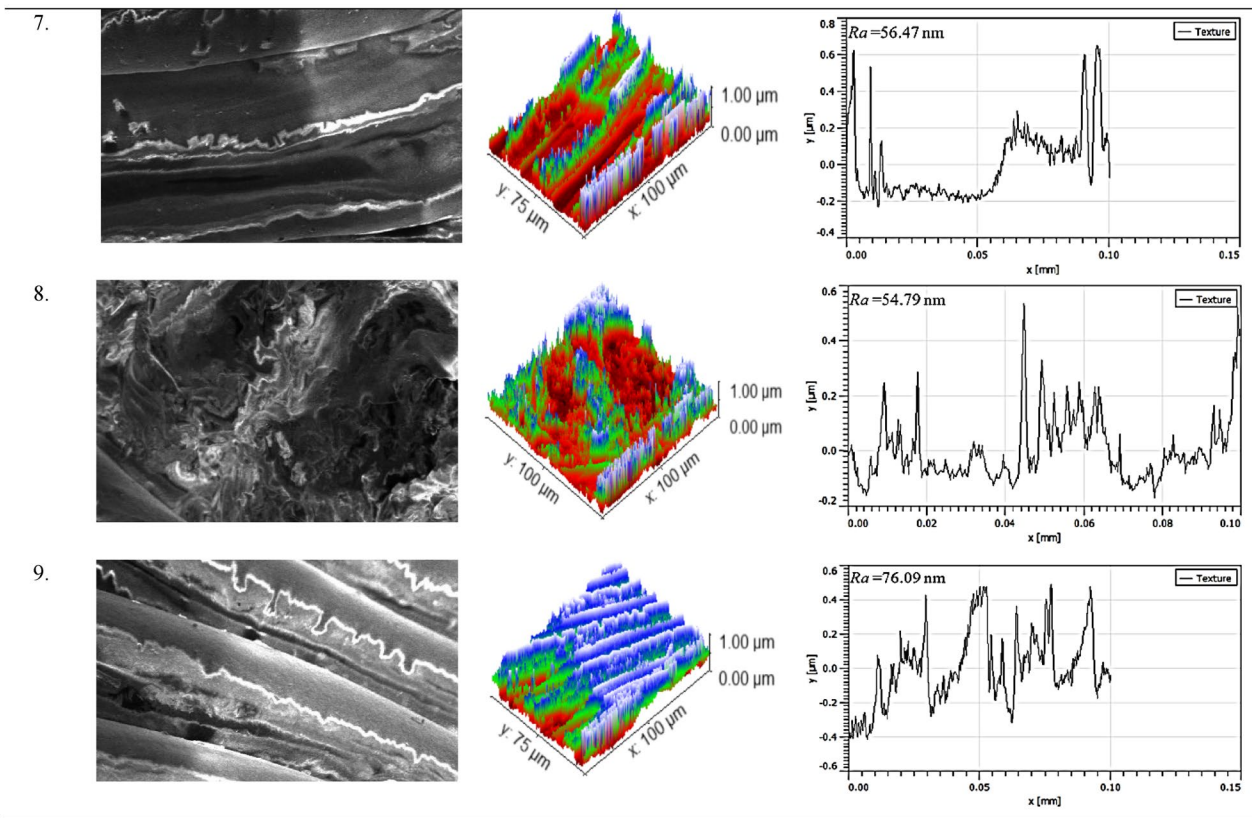
Exp. No.	SEM image of DC of MI AHT at 200×	3D rendered SEM image	R_a value at cut-off length 0.0380mm
1.			
2.			
3.			
4.			
5.			
6.			

Table 8 (continued)



deposition was noticed in AHT in comparison to higher density patterns, which may have resulted in better dimensional stability.

Finally using general linear model analysis and response optimization tool in Minitab 19 to identify the combination

of predictors for joint optimization (Fig. 11), multifactor optimization was performed based on observations of SN (obtained by Taguchi analysis of AHT and Δd_1) by giving 70% weightage to Δd_1 and 30% weightage to surface hardness (Table 9). The composite desirability was found as 0.824996 with the following optimized settings: low density, 180° orientation, and post-treatment temperature of 80 °C. The confirmatory experiments were performed as per proposed optimized settings and correspondingly $\Delta d_1 = 0.01$ mm and Shore *D* hardness AHT was noticed as 74. These results are in line with observations made by other investigators [10, 32–34, 44].

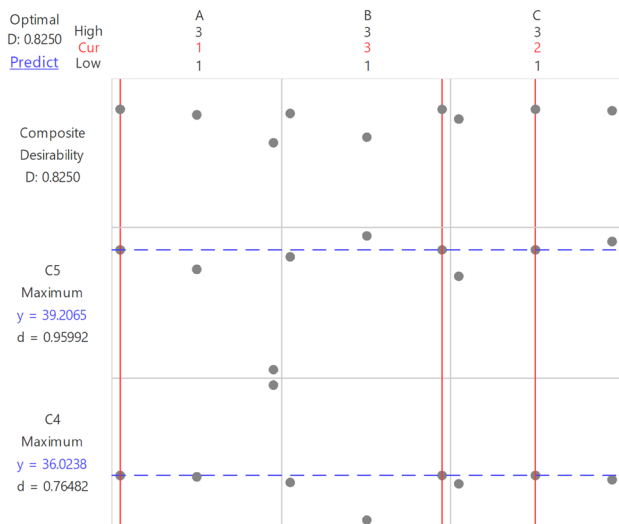


Fig. 11 Desirability plot for multiparameter optimization

5 Conclusions

Following are the conclusions from the present study:

1. The FFF patterns may be beneficial in the production (of master patterns) of DC for ST. Pattern density is the only relevant factor in determining the surface hardness of master patterns at the 95% confidence level, according to the experimental investigation, whereas other characteristics such as orientation angle and post-processing

Table 9 Composite desirability for multifactor optimization

Response	Goal	Lower	Target	Weight	Importance
SN ratio for $\Delta d1$ (dB)	Maximum	26.0206	40.0000	0.7	1
SN ratio for Shore D hardness AHT (dB)	Maximum	35.0410	37.4431	0.3	2
Solution					
	A B C Composite desirability				
	1 3 2 0.824996				

The decision for giving 70% weight to $\Delta d1$ and 30% weight to Shore D hardness has been made for the assembly fit of the respective crowns. The designer's perspective may vary to get a better fit and tolerance on case to case basis. It should be noted that the master patterns fabricated are showing a desirable range of hardness

temperature are not significant at the 95% confidence level.

- Similar observations were obtained for Δd of the master pattern. Pattern density is only relevant for Δd at the 95% confidence level, according to the results. Surface hardness and Δd measurements are consistent with R_a , surface texture profiles obtained by SEM investigations.
- In terms of FFF pre-and post-processing parameters for the printing of DC (for ST of dog), multifactor optimization reveals that the optimal settings from Δd and surface hardness perspective are orientation angle (180°), pattern density (low), and post-treatment temperature (80°C).
- The implementation of IT grade in preparation of DC for ST of dog may help in better assembly fit concerning a particular age group and breed of selected VP. The master pattern fabricated using the multi-factor optimization method will be used for IC for the preparation of DC.

The master pattern with recommended settings may be used for IC in the future. The influence of convergence angle in assembly fit may be explored in a simulative as well as the actual environment.

Acknowledgements The author(s) are thankful to DST (GoI) for providing research facilities under the FIST project (File No. SR/FST/COLLEGE/2020/997) and for financial support from DBT (GoI) (File No. 102/IFD/SAN/533/2017-18). Also special thanks to Precision Ceramic Artz, Dental Laboratory, Mohali, Punjab (India), Guru Angad Dev Veterinary and Animal Science University, Ludhiana, Punjab (India), Panjab University, Chandigarh (India), and National Institute of Technical Teachers Training and Research, Chandigarh (India) for lab facilities.

Declarations

Conflict of interests Authors have not any financial or non-financial interests that are directly or indirectly related to the work submitted for publication.

References

- Arif ZU, Khalid MY, Ahmed W, Arshad H (2022) A review on four-dimensional bioprinting in pursuit of advanced tissue engineering applications. *Bioprinting* 27:e00203
- Bae EJ, Jeong ID, Kim WC, Kim JH (2017) A comparative study of additive and subtractive manufacturing for dental restorations. *J Prosthet Dent* 118(2):187–193
- Khalid MY, Al Rashid A, Arif ZU, Ahmed W, Arshad H (2021) Recent advances in nanocellulose-based different biomaterials: types, properties, and emerging applications. *J Market Res* 14:2601–2623
- Singh S, Ramakrishna S, Singh R (2017) Material issues in additive manufacturing: a review. *J Manuf Process* 25:185–200
- Khalid MY, Arif ZU, Ahmed W (2022) 4D Printing: technological and manufacturing renaissance. *Macromol Mater Eng* 307(5):2200003
- Mitchell CA, Orr JF (2005) Engineering properties and performance of dental crowns. *Proc Inst Mech Eng* 219(4):245–255
- Eggbeer D, Bibb R, Williams R (2005) The computer-aided design and rapid prototyping fabrication of removable partial denture frameworks. *Proc Inst Mech Eng [H]* 219(3):195–202
- Lee S, Hong SJ, Paek J, Pae A, Kwon KR, Noh K (2019) Comparing accuracy of denture bases fabricated by injection molding, CAD/CAM milling, and rapid prototyping method. *J Adv Prosthodontics* 11(1):55–64
- Deradjat D, Minshall T (2017) Implementation of rapid manufacturing for mass customisation. *J Manuf Technol Manag* 28(1):95–121
- Pradhan SR, Singh R, Banwait SS, Singh S, Anand A (2021) 3D Printing assisted dental crowns for veterinary patients. *Ref Module Mater Sci Mater Eng*. <https://doi.org/10.1016/B978-0-12-820352-1.00153-X>
- Deb S (1998) Polymers in dentistry. *Proc Inst Mech Eng* 212(6):453–464
- Ma Q, Rejab MRM, Kumar AP, Fu H, Kumar NM, Tang J (2020) Effect of infill pattern, density and material type of 3D printed cubic structure under quasi-static loading. *Proc Inst Mech Eng Part C J Mech Eng Sci* 2020:1–19. <https://doi.org/10.1177/0954406220971667>
- Gupta Y, Iyer R, Dommeti VK, Nutu E, Rana M, Merdji A, Biswas JK, Roy S (2021) Design of dental implant using design of experiment and topology optimization: a finite element analysis study. *Proc Inst Mech Eng* 235(2):157–166
- Nsengimana J, Van der Walt J, Pei E, Miah M (2019) Effect of post-processing on the dimensional accuracy of small plastic additive manufactured parts. *Rapid Prototyping J* 25(1):1–12

15. Kumar N, Kumar JP (2019) Analysing the influence of raster angle, layer thickness, and infill rate on the compressive behaviour of EVA through CNC-assisted fused layer modelling process. *Proc Inst Mech Eng Part C J Mech Eng Sci* 2019:1–10. <https://doi.org/10.1177/954406219889076>
16. Dave HK, Patadiya NH, Prajapati AR, Rajpurohit SR (2019) Effect of infill pattern and infill density at varying part orientation on tensile properties of fused deposition modeling-printed poly-lactic acid part. *Proc Inst Mech Eng Part C J Mech Eng Sci* 2019:1–17. <https://doi.org/10.1177/954406219856383>
17. Keleş O, Blevins CW, Bowman KJ (2017) Effect of build orientation on the mechanical reliability of 3D printed ABS. *Rapid Prototyping J* 23(2):320–328
18. Capik I, Ledecy V, Sevcik A (2000) Tooth fracture evaluation and endodontic treatment in dogs. *Acta Vet Brno* 69(2):115–122
19. Rekow D, Thompson VP (2005) Near-surface damage—a persistent problem in crowns obtained by computer-aided design and manufacturing. *Proc Inst Mech Eng* 219(4):233–243
20. Suryawanshi AS, Behera N (2020) Tribological behavior of dental restorative composites in chewable tobacco environment. *Proc Inst Mech Eng* 234(10):1106–1112
21. Dawood A, Purkayastha S, Patel S, MacKillop F, Tanner S (2010) Microtechnologies in implant and restorative dentistry: a stroll through a digital dental landscape. *Proc Inst Mech Eng* 224(6):789–796
22. Pradhan SR, Singh R, Banwait SS (2020) A-frame work on crown fabrication for veterinary patients using 3D thermoplastic and metal printing. *Ref Module Mater Sci Mater Eng*. <https://doi.org/10.1016/B978-0-12-820352-1.00063-8>
23. Lemmons M, Beebe D (2019) Oral anatomy and physiology. *Wiggs's Vet Dentistry Principles Pract*. 2019:1–24
24. Ojeda J, Martínez-Reina J, García-Aznar JM, Domínguez J, Doblare M (2011) Numerical simulation of bone remodelling around dental implants. *Proc Inst Mech Eng* 225(9):897–906
25. Lo YJ, Chang WJ, Lee SY, Chang KJ, Lin CT, Huang HM (2009) Reductions in the effects of damping on stress concentration in premolars by post-endodontic restorations: a non-linear finite element study. *Proc Inst Mech Eng* 223(5):555–565
26. Coffman C, Visser C, Soukup J, Peak M (2019) Crowns and prosthodontics. *Wiggs's Vet Dentistry Principles Pract* 2019:387–410
27. Singh G, Singh R, Bal SS (2020) Investigations for partial denture casting by fused deposition modeling-assisted chemical vapour smoothing. *Assem Autom* 40(5):745–754
28. Ashley M, McCullagh A, Sweet C (2005) Making a good impression:(a'how to'paper on dental alginate). *Dent Update* 32(3):169–170
29. Al Qahtani MA, Alrefaie M, Altamimi A, Aljowyed I, Al Qahtani MA, AlQahtani A, Habib SR (2019) Evaluation of pre-alginate impression preparation methods in the surface accuracy of dental cast. *Saudi Dental J* 31(4):451–456
30. Hayashi K, Sachdeva AU, Saitoh S, Lee SP, Kubota T, Mizoguchi I (2013) Assessment of the accuracy and reliability of new 3-dimensional scanning devices. *Am J Orthod Dentofac Orthop* 144(4):619–625
31. Bansal M, Dhama SS (2009) 3D Scanning for reverse engineering-technological advancements, process overview, accuracy inspection, challenges, and remedies. *Int J Emerg Technol Eng Res* 10(5):33–40
32. Li S, Chen J, Kula KS (2019) Comparison of movement rate with different initial moment-to-force ratios. *Am J Orthod Dentofac Orthop* 156(2):203–209
33. Gagg G, Ghassemieh E, Wiria FE (2013) Analysis of the compressive behaviour of the three-dimensional printed porous titanium for dental implants using a modified cellular solid model. *Proc Inst Mech Eng [H]* 227(9):1020–1026
34. Nayak A, Jain PK, Kankar PK, Jain N (2021) Effect of volumetric shrinkage of restorative materials on tooth structure: a finite element analysis. *Proc Inst Mech Eng* 235(5):493–499
35. Häsler R, Schmid G, Ingervall B, Gebauer U (1997) A clinical comparison of the rate of maxillary canine retraction into healed and recent extraction sites—a pilot study. *Eur J Orthod* 19(6):711–719
36. Clift SE, Fisher J, Watson CJ (1993) Stress and strain distribution in the bone surrounding a new design of dental implant: a comparison with a threaded Branemark type implant. *Proc Inst Mech Eng* 207(3):133–138
37. Genovese K, Lamberti L, Pappalettere C (2006) Structural behaviour of endodontically treated teeth under thermomechanical loading. *Proc Inst Mech Eng* 220(8):909–928
38. Rees JS (2006) The biomechanics of abfraction. *Proc Inst Mech Eng* 220(1):69–80
39. Singh JP, Singh R (2009) Investigations for statistically controlled rapid casting solution of low brass alloys using three-dimensional printing. *Int J Rapid Manuf* 1(2):208–221
40. DiBenedetto AT (1987) Prediction of the glass transition temperature of polymers: a model based on the principle of corresponding states. *J Polym Sci Part B: Polym Phys* 25(9):1949–1969
41. Singh P, Pungotra H, Kalsi NS (2020) Parametric optimization of deep cryogenic treatment for the wear response of implant material UNS R56700: Taguchi's approach. *Proc Inst Mech Eng* 234(1):61–73
42. Rahman M, Schott NR, Sadhu LK (2016) Glass transition of ABS in 3D printing. In: *COMSOL Conference*, Boston, pp 1–5
43. Yazdi MH, Lee-Sullivan P (2009) Determination of dual-glass transition temperatures of a PC/ABS blend using two TMA modes. *J Therm Anal Calorimetry* 96(1):7–14
44. Pradhan SR, Singh R, Banwait SS (2021) On crown fabrication in prosthetic dentistry of veterinary patients: a review. *Adv Mater Process Technol* 2021:1–20. <https://doi.org/10.1080/2374068X.2021.1970991>

Publisher's Note Springer Nature remains neutral with regard to jurisdictional claims in published maps and institutional affiliations.